ADDING SENSITIVITY TO 21CM INTEFEROMETRIC PROBES OF REIONIZATION BY OPTIMIZING CHOICE OF BASELINES

Yunfan Gerry Zhang [1], Aaron R. Parsons[12]

[1]Astronomy Dept., U. California, Berkeley, CA
[2]Radio Astronomy Lab., U. California, Berkeley, CA

ABSTRACT

We introduce an accurate method to extract additional sensitivity from data of redundant radio arrays. Using the 64 element version of Precision Array for Probing the Epoch of Reionization (PAPER-64), we illustrate how our method finds optimal baselines to cross correlate, including baselines that are slightly different in length and orientation. We predict the sensitivity improvements of including each baseline pairs. The extremely natural and simple implementation of this method would increase the sensitivity of PAPER-64 by up to [50] percent.

1. INTRODUCTION

The epoch of reionization, or cosmic dawn represents the last key stage of the universe's early evolution. Study of this event stands at the intersection of cosmology and astrophysics. Understanding this event is important not only as a scientific goal of its own, but also because it potentially provides crucial information to fundamental nature of inflation, neutrino mass and phenomenology of the first stars and galaxies alike (e.g. ?).

Arguably the most promising observational probe of the epoch of reionization comes from measurement of the "spin-flip" transition of neutral hydrogen of characteristic wavelength 21cm Furlanetto et al. (2006); Pritchard & Loeb (2012). While probes such as quasar spectra rely on emission and scattering of free electrons, and are thus limited to the lower redshifts after the completion of reionization, the 21cm line directly probes the abundance and distribution of neutral hydrogen, and thus would potentially shed light on all stages of reionization. Radio interferometry efforts to measure the 21cm power spectrum has been a top priority in recent years of astronomy. Current generation instruments include the Precision Array for Probing the Epoch of Reionization (PAPER) Ali et al. (2015); Parsons et al. (2014), Murchison Widefield Array (MWA) Ewall-Wice et al. (2016), Low Frequency Array (LOFAR) van Haarlem, M. P. et al. (2013), and next generation instruments such as the Hydrogen Epoch of Reionization Array (HERA) (e.g. ?Dillon & Parsons (2016); Neben et al. (2016); Ewall-Wice et al. (2016)) and the Square Kilometer Array Low (SKA low) (e.g. Mesinger et al. (2015)) are under construction.

One of the main challenges of interferometric observations of cosmic 21cm line is the foreground contamination. Both sources within our galaxy, and to a lesser distant sources outside of our galaxy emit radio contaminations (via for example synchrotron processes) up to five orders of magnitude stronger than the reionization signal. There are two common methods to deal with the foreground contamination. In the first, sometimes called the foreground removal technique, individual sources are identified and removed in the image domain. The other technique, commonly referred to as 'foreground avoidance', makes use of the fact that most common foreground contaminations have a smooth spectrum, and thus is constrained to a Fourier domain "foreground wedge" Liu et al. (2014a,b). Thus contamination can be avoided by restricting our observation to "outside the wedge", where the data is currently noise dominated. The main challenge of using the avoidance technique is thus the sensitivity, or the signal to noise ratio. This is the motivation for the design of the maximum redundancy arrays such as PAPER and HERA. While traditional imaging arrays focus on Fourier mode uv coverage, the redundant arrays have many tightly packed antennas at equal spacing. Since baselines of the same length and orientation measure the same Fourier modes on the sky, the maximum redundancy arrays is able to increase the signal to noise ratio by averaging over measurements of the same baseline. Ali et al. (2015) provides the newest upper limit to the power spectrum measurements with the PAPER-64 data. From some models we roughly expect that the sensitivity required for detection is a factor of 10 away. This paper explores a new technique to add sensitivity to the analysis of redundant arrays, by making use of the earth's rotation. This technique can be applied to redundant arrays such as PAPER and HERA to increase the sensitivity by up to a factor of [1.5].

The earth's rotation causes the baselines to pick up different modes of the sky with time. This effect is used extensively to improve uv coverage in imaging with minimum redundancy arrays. In a maximally redundant array, baselines that are slightly different rotate into each

other at a time delay. Here we present a method to improve the sensitivity of the maximum redundancy arrays by considering the uv redundancy of different baselines at a time lag.

Baselines of the same length and orientation are traditionally called "redundant baselines", because they measure the same Fourier mode in the sky. In order to eliminate confusion and ambiguity, we shall introduce slightly different terminology. We'll call baselines that are the same length and orientation "equivalent baselines", inspired by the mathematical notion of equivalency classes. Two equivalent baselines will be redundant with each other simultaneously at all times. Some non-equivalent baselines can also be redundant if their respected time series is shifted with respect to one another by a certain delay. In other words, one baseline can be "rotated into" another. We call these "near-equivalent baselines". It is our goal to a) identify the near-equivalent baselines that give good redundancy, b) to find the optimal time offset for a given pair of baselines, and c) to quantify the sensitivity improvement associated with cross multiplying such a pair of near-equivalent baselines. In section 2 we explain the theoretical basis for this cross multiplication. In section 3 we present details of the numerical implementation of this technique. In section 4 we discuss the expected sensitivity improvement with this method and with section 5 we conclude.
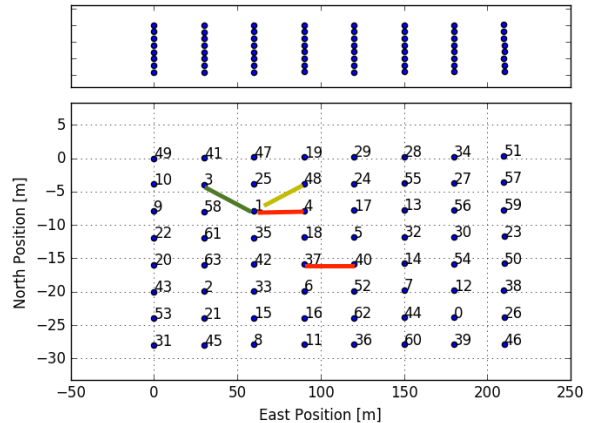
2. METHOD

2.1. *Rough Idea*

Figure 1. The PAPER-64 layout. Each blue dot corresponds to the location of an antenna. Top panel shows the antenna positions drawn to scale, bottom panel show the antenna labels and distances. The numbering of the antennas the bottom panel are original labels during instrument assembly and does not bear significant meaning. Baselines corresponding to the same separations are called equivalent. In the bottom panel, the two baselines labeled with the red arrow are equivalent, with separation denoted by sep1,0, for the antennas are separated by 1 unit east and 0 unit north. Similarly, the baselines labeled with the yellow and green arrows are examples of sep1,1 and sep-1,1, respectively. Note sep1,0 and sep-1,0 for example are the same baselines and should not be counted twice.

We shall use the 64-antenna PAPER array to demonstrate. The PAPER-64 array is located in the Karoo desert in South Africa (30:43:17.5 S, 21:25:41.8 E). The layout pattern with antenna labels are show in Fig. 1. We see the antenna spacing in North-South directions are comparatively close (4m), so that baselines such as 0_44 and 0_7 are very close to equivalent. In the bottom panel, the two baselines labeled with the red arrow are equivalent, with separation denoted by sep1,0, for the antennas are separated by 1 unit east and 0 unit north. Similarly, the baselines labeled with the yellow and green arrows are examples of sep1,1 and sep-1,1, respectively. Note sep1,0 and sep-1,0 for example are the same baselines and should not be counted twice. Turns out antennas in purely north-south baselines are close enough to induce cross talks, and hence are not suitable for use. The original PAPER-64 analysis thus used three classes of baselines, sep1,0, sep1,1 and sep-1,1 Ali et al. (2015). There each of these classes of baselines are cross multiplied to itself. We shall see that in addition these baseline classes can be cross multiplied with a time offset.

Given a point source on the sky, each baseline maps the source to a point in uv plane. As the earth rotates with respect to the source, the point traces out tracks in the uv-plane. The uv tracks of PAPER-64 over 7.2 hours, at 0.15GHz, for a source that passes through zenith, are shown in Fig. 2.
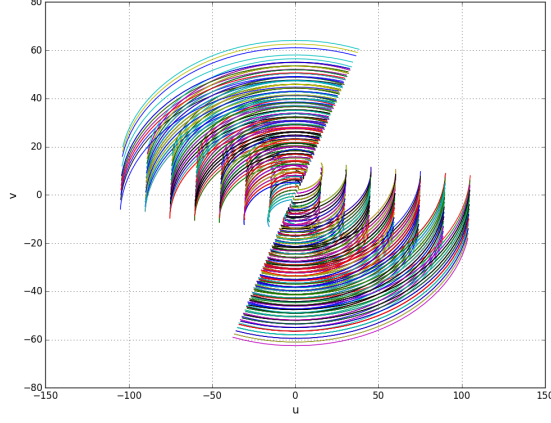
Figure 2. Tracks of PAPER-64 for a hypothetical source that passes through zenith. These tracks are traced out over 0.3 sidereal days, or roughly 7.2 hours. Color represents different baselines. Frequency is $\nu = 0.15$GHz. As the earth rotates, tracks are traced out counterclockwise.

Roughly speaking, we can identify redundancy of near-equivalent baselines as crossings of the uv tracks. Although this is a valid quick method to identify some baselines to cross-multiply, we find that it is not accurate enough for time offset determination. The reason is, for wide beam antennas such as PAPER-64, the sources are not point-like. In other words, when tracks of one point of the sky are crossing in uv-plane, those corresponding to another is not. To accurately constrain redundancy we must take into account of finite beam width. A more rigorous treatment is thus required. We show the beam of PAPER-64 in Fig.3 for reference:
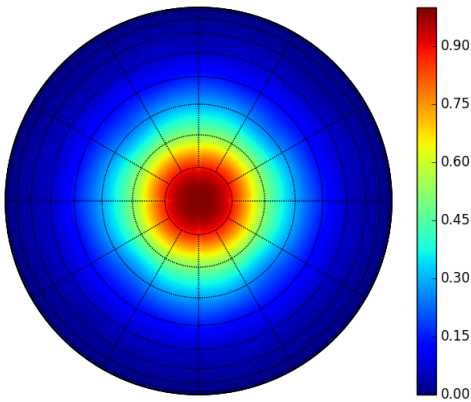

Figure 3. Beam of PAPER-64. Shown here is the values of A (Eq. (1)) for frequency of $\nu = 150$MHz. Notice A is a "baseline's beam". Since all antennas in PAPER-64 have the same beam, A here is just the square of an antenna beam, and is normalized to 1 at the center. The circles centered around zenith (center of beam) here are spaced 10 degrees apart. Such a wide beam limits the accuracy of the uv track-crossing as a method of redundancy search.

2.2. Formalism

Below we shall derive theoretical expectations of cross multiplications of two near-equivalent baselines. More precisely we shall relate the product of visibilities of two different baselines to the power spectrum.

We take the visibility as commonly defined in the literature (e.g. Parsons et al. (2012a)):

$$V_\nu(b) = \int d\Omega A_\nu(\hat{s})\phi(\nu)I_\nu(\hat{s}) \exp\left[-2\pi i \frac{\nu}{c} b \cdot \hat{s}\right],$$
$$\approx \frac{2k_B}{\lambda^2} \int d\Omega A_\nu(\hat{s})\phi(\nu)T(\hat{s}) \exp\left[-2\pi i \frac{\nu}{c} b \cdot \hat{s}\right],$$
(1)

Here λ is a mean wavelength, $\boldsymbol{b}$ is the baseline length, $\hat{s}$ and Ω are a direction in the sky and its corresponding solid angle. A_ν is the (frequency dependent) beam, and I is the specific intensity, which has been related to T, the brightness temperature in the Rayleigh-Jeans limit. $\phi(\nu)$ is the frequency band profile. For PAPER-64, for example, the bands studied are roughly a top-hat from 144MHz to 154 MHz.

We define the delay transformed visibility Parsons et al. (2012b):

$$V(b,\tau) = \int d\nu V_\nu(b)\phi(\nu) \exp\left[-2\pi i\nu\tau\right],$$
$$= \frac{2k_B}{\lambda^2} \int d\Omega d\nu A(\hat{s},\nu)\phi(\nu)T(\hat{s},\nu) \exp\left[-2\pi i\nu\left(\frac{b\cdot\hat{s}}{c} + \tau\right)\right].$$
(2)

Eq. (2) expresses the delay-transformed visibility as an integral over observation coordinates $\hat{s}$ and ν. Ultimately, we would like to relate the data, collected with coordinates $\hat{s}$ and ν, to the power spectrum, written with cosmological coordinates $\boldsymbol{r}$ and $\boldsymbol{k}$. We start by noticing that [Gerry: change all r and k into bold]

$$r = \frac{c}{H_0} \int_0^z \frac{dz'}{E(z')},$$
$$\approx \frac{c}{H_0} \int_0^{z_0} \frac{dz'}{E(z')} - \frac{c(1+z)^2}{\nu_{21}H_0E(z)}(\nu - \nu_0),$$
(3)
$$\equiv D_c - Y\Delta\nu,$$

where $\nu_{21} = 1420MHz$ is the 21cm transition rest frequency, ν_0 a reference central frequency with corresponding redshift z_0, and

$$E(z) = \sqrt{\Omega_m(1+z)^3 + \Omega_\Lambda}.$$
(4)

Inverting for ν:

$$\nu = \frac{D_c - r}{Y} + \nu_{21}.$$
(5)

Thus $d\nu = -dr/Y$ and $d^3r = -X^2Y d\Omega d\nu$.

We can thus rewrite the delayed transformed visibility as

$$V(b,\tau) = \frac{1}{X^2Y} \int_H d^3r A(\vec{r})\phi(r)I(\vec{r}) \exp\left[-2\pi i \left(\frac{b}{c}\cdot\hat{r} + \tau\right)\nu_r\right].$$
(6)

Here $(r_x, r_y, r_z) = (X\hat{s}_x, X\hat{s}_y, Y\nu)$, and $(Xk_x, Xk_y, Yk_z) = \frac{2\pi}{c}(b_x, b_y, \eta)$ relate the cosmological

coordinates r and k to the measured coordinates. We have written ν_r to remind us that ν and r are related by Eq. (5). The beam reception pattern A is dimensionless, normalized to 1 at its peak (zenith), and we assume it to be the same for all baselines.

With a time offset, the beam pattern has moved relative to the sky. Here we choose to fix the sky, and denote the rotated coordinates of the beam pattern with the operator Γ. With implicit bounds of integrals from $-\infty$ to ∞, we have:

$$
\begin{aligned}
&\langle V^*(b,\tau)V(b',\tau')\rangle \\
&= \left(\frac{2k_B}{X^2Y\lambda^2}\right)^2 \int d^3r d^3r' \left(\langle T^*(r)T(r')\rangle\right) A^*(r)A(\Gamma r')\Phi_{b,\tau}(r,\Gamma r'), \\
&= \left(\frac{2k_B}{X^2Y\lambda^2}\right)^2 \int d^3r d^3r' \left(\int \frac{d^3\kappa}{(2\pi)^3}\frac{d^3\kappa'}{(2\pi)^3}\langle T^*(\kappa)T(\kappa')\rangle e^{-i(\kappa r-\kappa'r')}\right) A^*(r)A(\Gamma r')\Phi_{b,\tau}(r,\Gamma r'), \\
&= \left(\frac{2k_B}{X^2Y\lambda^2}\right)^2 \int d^3r d^3r' \left(\int \frac{d^3\kappa}{(2\pi)^3}P(\kappa)e^{-i\kappa(r-r')}\right) A^*(r)A(\Gamma r')\Phi_{b,\tau}(r,\Gamma r'), \\
&= \left(\frac{2k_B}{X^2Y\lambda^2}\right)^2 \int d^3r d^3r' \xi(r-r')A^*(r)A(\Gamma r')\Phi_{b,\tau}(r,\Gamma r'), \\
&\approx \left(\frac{2k_B}{X^2Y\lambda^2}\right)^2 P(k_{b,\tau}) \int d^3r d^3r' \delta_D^{(3)}(r-r')A^*(r)A(\Gamma r')\Phi_{b,\tau}(r,\Gamma r'), \\
&= \left(\frac{2k_B}{X^2Y\lambda^2}\right)^2 P(k_{b,\tau}) \int d^3r |A^*(r)A(\Gamma r)||\phi(\nu_r)|^2 \exp\left[-i2\pi\nu_r\left(\hat{r}\cdot\frac{b}{c}-\hat{\Gamma r}\cdot\frac{b'}{c}\right)\right], \\
&= \left(\frac{2k_B}{\lambda^2}\right)^2 P(k_{b,\tau}) \int \frac{d\Omega d\nu}{X^2Y}|A^*(\hat{s},\nu)A(\hat{\Gamma s},\nu)||\phi(\nu)|^2 \exp\left[-i2\pi\nu\left(\hat{s}\cdot\frac{b}{c}-\hat{\Gamma s}\cdot\frac{b'}{c}\right)\right],
\end{aligned}
\tag{7}
$$

where in transition from cosmological coordinates back to observing coordinates we have written $\hat{r}\equiv\hat{s}$, and

$$
\Phi_{b,\tau}(r,\Gamma r') = |\phi^*(\nu_r)\phi(\nu_{r'})| \exp\left[-i\frac{2\pi}{c}\left(b\cdot\nu_r\hat{r}-b'\cdot\nu_{r'}\Gamma\hat{r'}\right)\right]\exp\left[-i2\pi\tau\left(\nu_r-\nu_{r'}\right)\right].
\tag{8}
$$

The second to third line of Eq.(7) follows from assumption of Gaussian random sky, and the third to fourth line follows from the assumption that the 3D power spectrum varies negligibly over the region of interest so that $\hat{P}_{21}(k+k_2)\approx\hat{P}_{21}(k)$. Since Γ is a sky rotation, it doesn't affect ν, hence we have taken ν_r outside the parenthesis. Notice that the phase factor $\exp\left[-i2\pi\eta\left(\nu-\nu'\right)\right]$ drops out in the end.

Finally, since the beam pattern and bandwidth are given in $\hat{s}$ and ν, we convert the integral back to these coordinates to get the general relation between the delay-transformed visibilities and the power spectrum:

$$
\begin{aligned}
&\langle V^*(b,\tau)V(b',\tau')\rangle \\
&= \left(\frac{2k_B}{\lambda^2}\right)^2 P(k_{b,\tau}) \int \frac{d\Omega d\nu}{X^2Y}|A^*(\hat{s},\nu)A(\hat{\Gamma s},\nu)||\phi(\nu)|^2 \\
&\qquad \exp\left[-i2\pi\nu\left(\hat{s}\cdot\frac{b}{c}-\hat{\Gamma s}\cdot\frac{b'}{c}\right)\right].
\end{aligned}
\tag{9}
$$

So roughly speaking the cross multiplications of visibilities at a time delay in uv-space is proportional to the power spectrum times the Fourier transform of the cross multiplied beam pattern. We can then in principle combine information from different baseline pairs if

we correct for the phase and normalization. As a check, when applied to equivalent baselines, $b=b'$, $\hat{s}=\hat{\Gamma s}$, and Eq.(9) reduces to Eq.(B9) of Parsons et al. (2014).

If this result is robust, then we can achieve all our goals stated in the introduction, i.e. to identify candidate baseline pairs, to find the optimal time offset, and to quantify the sensibility, by computing the integral in Eq.(9) for various time offsets. Thus we shall first test its robustness numerically.

3. ANALYSIS

3.1. *Numerical Test*

As the earth rotates, a point source traces out a track in UV plane for a given baseline. Shown in Fig. 2 are the rotation tracks for a source that passes through zenith for the baselines of PAPER-64. As we mentioned earlier, crossings of these tracks are approximate, and only approximate points of maximum redundancy of near-equivalent baselines, because of the wide field of view of the PAPER beam, shown in Fig.3).

In practice, we first implement a search algorithm that grids the uv plane and search for intersections these tracks, then fine tune the time delay by computing a) cross correlated visibilities from simulated random sky, and b) theoretical proportion factor from Eq. (7) for a

range of time delays. It is also worth pointing out that the near-redundant pairs is not only useful at a particular time corresponding to the crossing. The search algorithm uses a fiducial point source in the sky to find the offset, and all time-stamps separated by this offset corresponds to UV-track crossing of a point in the sky, and thus all data of the two baselines can be utilized.

At the optimal time separation, the integral in Eq. (9) is maximized. We expect the two beams to have to same fringe pattern (frequency and phase). Due to the time delay, however, the beam center would be slightly shifted with respect to each other. This we show in Fig. [insert]. The left and middle panels show the beam fringe patterns for baselines sep0,1 and sep1,1, delayed by 0.0325 days, and the right panel shows their cross product. The fringe pattern indeed cancels out as we expect.
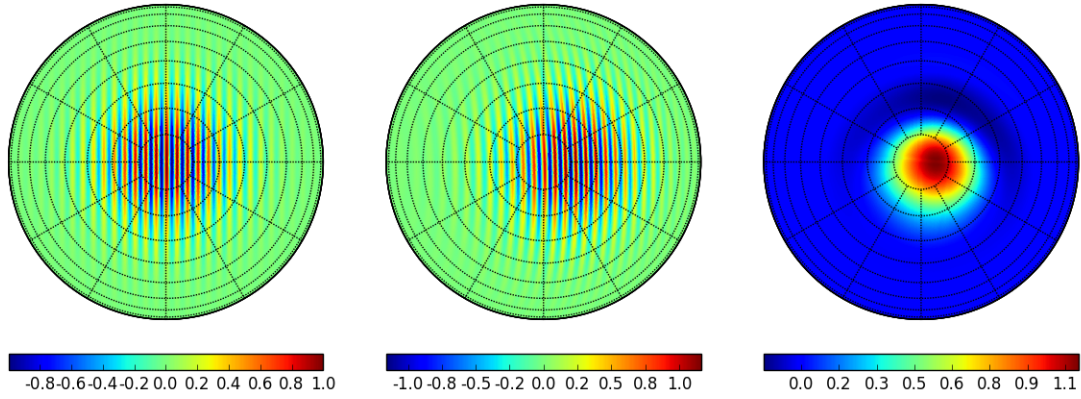

Figure 4. Beam fringe pattern of sep1.0(left), sep1,1 at a time delay (middle), and their conjugate product. Frequency of $\nu = 0.15$GHz is chosen.

Below we go into a little more details on the numerical techniques we used to obtain the results.

3.2. *Track crossing search [skip all together?]*

The crossing algorithm sets up grids on the UV-plane, creates a point source that passes through zenith, and searches for intersections of the UV tracks. The search compares each track to each other track to locate the closest approaches. To optimize performance, the algorithm first sets up coarse grids, locates the cells that contain data points from more than one tracks, then fine-grains the cell to determine the points of closest approach. Fig [insert] illustrates this procedure. After all the crossings have been identified, we rank the crossings by computing the proportion factor in Eq. (7). This algorithm is mainly used to determine which baselines to cross correlate, and give a rough estimate of the time offset. We indeed find that baselines sep0,1 and sep1,1 give the closest approach with a time offset of roughly 0.03 sidereal days. In reality, a wide beam samples a patch of sky, not just a point source. And thus the real UV representation of a baseline is the track convolved with an appropriate point spread function. Accounting for these factors accurately in this context is difficult.

Thus for accurate determination of the time offset, we resort to two other methods.

3.3. *Gaussian sky simulation*

Having found the pairs of baselines to cross-correlate, and a rough estimate of the time offset, we make a more accurate determination of the time offset. Here we take N random realizations of the sky on a healpix map[1]. For each realization, each pixel is given a Gaussian random value of brightness temperature. We then rotate the baseline positions with the appropriate rotation matrix, recording the visibilities, for each baseline, as given in Eq. 1 [2]. The resulting visibilities for the two baselines are then convolved via the Fourier convolution theorem, to obtain values of the cross correlation as a function of time-offset. The peak of the curve then corresponds to maximum redundancy. The accuracy of this result is limited by (simulated) cosmic variance and finite spacial resolution, and hence can be beat down by averaging over a large number of universes. A numerical estimate of the error of the peak height with $N = 1$ is $\lesssim 20\%$, and thus with $N = 2500$, we achieve an error of peak height $< 0.5\%$. An example is shown in Fig. [insert]

3.4. *Theoretical determination*

To test our understanding of the time-offset, and to verify our derivation in Eq. (7) makes sense, we must check the curve obtained in Fig. [insert] against one from the multiplicative factor in Eq. (7). In particular, we would really like to compare the peak location as well as height. For the latter, the most useful information comes in its comparison with that of an equivalent baseline. Thus in Fig. [insert] below we show on the left comparison of the convolution of an equivalent baseline, normalized to 1 at the peak, whose location is at 0 offset as expected. On the right we show comparison of the baseline pair found in the grid search. The peaks are normalized with the same factor as the peak height on the left, i.e. the two plots have thus the same scale on the vertical axis. The height of the plot on the right thus quantifies the added sensitivity.

---

[1] We use functionalities in the python package AIPY for healpix mapping as well as coordinate transforms.

[2] As a caveat, there are two obvious ways to achieve the rotation. One can either fix the sky and rotate the baselines, or the other way around. We found however, that we must not physically rotate the sky map, for the numerical roundoffs due to finite resolutions of the map turns out to be significant. Thus we let the sky, represented by the healpix map, be fixed, and rotate the baselines.
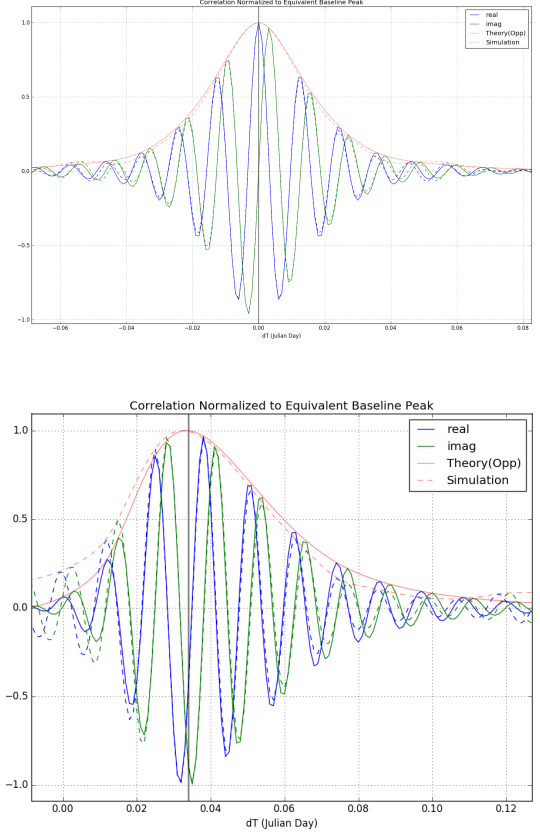

Figure 5. The PAPER-64 layout. Top panel shows the antenna positions drawn to scale, bottom panel show the antenna labels and distances.

3.5. *Expected Sensitivity Contributions*

In section (3.3) and (3.4) we showed the delays and amount of overlap for the baselines with separation sep10 vs sep11. In the top panel of Fig. (3.5) below we show the peak heights and locations for a variety of baseline combinations. We see that baseline pairs that have crossings at a smaller time delay tend to have higher correlations. In other words, correlation peaks that are closer to zero time lag are higher. This is expected since a) the longer the time delay, the more the antennas have moved with respect to the sky and hence the less overlaps in patch of sky surveyed, b) smaller optimal time-offset corresponds to smaller differences in orientation, and hence in length of baselines in PAPER-64.
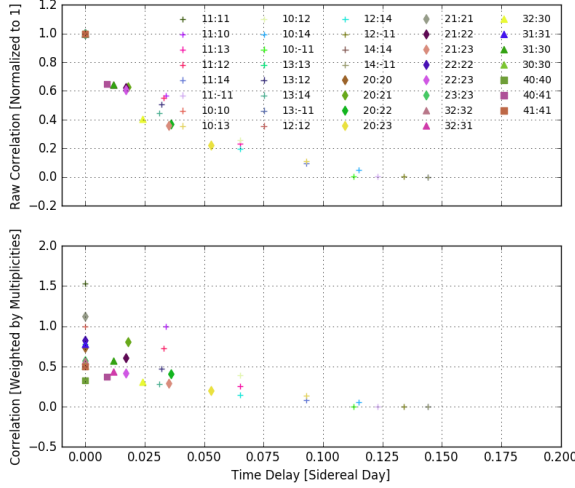
Figure 6. Relative sensitivity contributions of selected baseline combinations in PAPER-64. In the legend m,n:p,q denotes cross multiplying PAPER-64 baselines of east-west, north-south separations (m,n) and (p,q) respectively. The top panel shows the peak height (degree of correlation) of each baseline combination, while the bottom panel multiplies the heights by the corresponding multiplicities as in Eq. (11), and in some cases an extra factor of 2 (explained in text). In weighting by the multiplicity (bottom), we have chosen to fix the sensitivity contribution of 1,0:1,0 to unity.

To determine that actual relative contribution to sensitivity of these baseline pairs, we have to take into account of the multiplicities of these baselines, or the size of the equivalency classes in a mathematical language. By these we mean how many physical antenna pairs have the same length and orientation. Looking at Fig. 1 we see for example sep1,0 will have higher redundancy than sep2,0, or sep1,1. The latest release of PAPER-64 data uses baselines sep-1,1, sep0,1 and sep1,1 Ali et al. (2015), and achieved a 2σ upper limit of $22.4 mK^2$. There, the three sets of equivalent baselines are only cross multiplied by itself. Assuming that each baseline delivers the same quality of data (i.e. they have the same height of correlation peaks, which is in our normalization equal to unity), the relative contribution to sensitivity can be estimated.

First we can average of the visibilities of the baselines of the same separations. Since PAPER-64 has 8 by 8 antenna configuration, there are $(8-|m|)\times(8-|n|)$ copies of the baseline sepm,n. This means that if we add visibility measurements of all these equivalent baselines, we get a factor of $\sqrt{(8-|m|)\times(8-|n|)}$ reduction in noise level. The sensitivity contribution of sepm,n, being the signal to noise ratio of the power spectrum, is thus proportional to $(8-|m|)\times(8-|n|)$. Next we can average over the power-spectrum taken from baselines of the different separations. Thus the total cumulative sensitivity is given by

$$\frac{P_S}{P_N} \propto \sqrt{\sum_{(n,m)} \left((8-|m|)\times(8-|n|)\right)^2}, \quad (10)$$

where the sum is only over pairs of m and n. If we now include power spectrum from cross-multiplications of near-equivalent baselines of types sepm,n and sepm',n', we get a general cumulative sensitivity:

$$\frac{P_S}{P_N} \propto \sqrt{\sum_{(n,m,n',m')} \Omega_{mnm'n'} \left((8-|m|)(8-|n|)(8-|m'|)(8-|n'|)\right)}, \quad (11)$$

where Ω is the correlation peak height show in top panel of Fig. (3.5), and the sum is again only over tuples of m,n,m',n'. This form now includes the equivalent baselines in Eq. (10), with $\Omega_{m=m',n=n'} = 1$. Shown in the bottom panel of Fig. (3.5) is the peak heights weighted by this multiplicity factor (before taking the square root), with one difference. The difference is, since we have "folded over" the negative time delays, we have combined baseline pairs that are identical modulus parity, or in other words are mirror images of each other, by summing over them to get an extra factor of two. For example, instead of plotting 1,1:1,1 and 1,-1:1,-1 separately, we plot 1,1:1,1 with twice the multiplicity. Similarly, baseline pairs such as 1,0:1,1 also get the factor of 2 because they are identical to 1,0:1,-1. Baseline pairs such as 1,0:1,0, or 1,1:1,-1 do not get the factor of 2 because their mirror images are themselves.

4. CONCLUSION

REFERENCES

Ali, Z. S., Parsons, A. R., Zheng, H., et al. 2015, The Astrophysical Journal, 809, 61

Dillon, J. S., & Parsons, A. R. 2016, ArXiv e-prints, arXiv:1602.06259

Ewall-Wice, A., Dillon, J. S., Hewitt, J. N., et al. 2016

Ewall-Wice, A., Bradley, R., DeBoer, D., et al. 2016, ArXiv e-prints, arXiv:1602.06277

Furlanetto, S. R., Oh, S. P., & Briggs, F. H. 2006, Physics Reports, 433, 181

Liu, A., Parsons, A. R., & Trott, C. M. 2014a, Phys. Rev. D, 90, 023018

—. 2014b, Phys. Rev. D, 90, 023019

Mesinger, A., Ferrara, A., Greig, B., et al. 2015, Advancing Astrophysics with the Square Kilometre Array (AASKA14), 11

Neben, A. R., Bradley, R. F., Hewitt, J. N., et al. 2016, ArXiv e-prints, arXiv:1602.03887

Parsons, A., Pober, J., McQuinn, M., Jacobs, D., & Aguirre, J. 2012a, The Astrophysical Journal, 753, 81

Parsons, A. R., Pober, J. C., Aguirre, J. E., et al. 2012b, The Astrophysical Journal, 756, 165

Parsons, A. R., Liu, A., Aguirre, J. E., et al. 2014, The Astrophysical Journal, 788, 106

Pritchard, J. R., & Loeb, A. 2012, Reports on Progress in Physics, 75, 086901

van Haarlem, M. P., Wise, M. W., Gunst, A. W., et al. 2013,
AA, 556, A2